Inverse modeling of geochemical and mechanical compaction in sedimentary basins through Polynomial Chaos Expansion

By G. Porta[1], L. Tamellini[2,3], V. Lever[1], M. Riva[1,4]

[1]Dipartimento di Ingegneria Civile e Ambientale Politecnico di Milano, Piazza L. Da Vinci 32, 20133 Milano, Italy

[2] MOX, Dipartimento di Matematica, Politecnico di Milano, Piazza L. Da Vinci 32, 20133 Milano, Italy

[3] CSQI-MATHICSE, Ecole Polytechnique Fédérale de Lausanne, Station 8, CH 1015, Lausanne, Switzerland

[4]Department of Hydrology and Water Resources, University of Arizona, Tucson, Arizona 85721, USA

This article has been accepted for publication and undergone full peer review but has not been through the copyediting, typesetting, pagination and proofreading process which may lead to differences between this version and the Version of Record. Please cite this article as an 'Accepted Article', doi: 10.1002/2014WR015838

ABSTRACT

We present an inverse modeling procedure for the estimation of model parameters of sedimentary basins subject to compaction driven by mechanical and geochemical processes. We consider a sandstone basin whose dynamics are governed by a set of unknown key quantities. These include geophysical and geochemical system attributes as well as pressure and temperature boundary conditions. We derive a reduced (or surrogate) model of the system behavior based on generalized Polynomial Chaos Expansion (gPCE) approximations, which are directly linked to the variance-based Sobol indices associated with the selected uncertain model parameters. Parameter estimation is then performed within a Maximum Likelihood (ML) framework. We then study the way the ML inversion procedure can benefit from the adoption of anisotropic polynomial approximations (a-gPCE) in which the surrogate model is refined only with respect to selected parameters according to an analysis of the nonlinearity of the input-output mapping, as quantified through the Sobol sensitivity indices. Results are illustrated for a one-dimensional setting involving quartz cementation and mechanical compaction in sandstones. The reliability of gPCE and a-gPCE approximations in the context of the inverse modeling framework is assessed. The effects of (a) the strategy employed to build the surrogate model, leading either to a gPCE or a-gPCE representation, and (b) the type and quality of calibration data on the goodness of the parameter estimates is then explored.

1. INTRODUCTION

Interaction of sediment compaction processes with subsurface fluid flow has been studied in the presence of a wide set of observed phenomena including compaction-driven brine and/or saltwater flow at deep locations [*Kreitler,* 1989], transport of tracer concentrations in shallow sediments [*Hurwitz et al.*, 2000; *Bonnesen et al.*, 2009], build-up of fluid pressure [*Jiao and Zheng*, 1998; *McPherson and Bredehoeft*, 2006], hydrocarbon generation and migration [e.g., *Tuncay and Ortoleva*, 2004; *Taylor et al.,* 2010], land subsidence due to groundwater and/or hydrocarbons withdrawal [*Gambolati et al.*, 1991, 2000; *Hoffman et al.*, 2003] and formation of ore deposits [*Wieck et al.* 1995]. Evolutionary scales of compaction processes can range over several orders of magnitude, mainly depending on the driving physical sources. For instance, land subsidence is often caused by human over exploitation of subsurface resources and is observed on time intervals spanning decades. On the other hand, natural compaction phenomena, including mechanical and geochemical processes taking place in sedimentary basins, are associated with geological time scales, i.e. millions of years [*Wangen,* 2010]. Mechanical compaction is due to variations of effective stress caused by increased load of overlying sediments after deposition. Stress change induces grain rearrangement and porosity reduction with increasing depth. Geochemical compaction has also a marked influence on the evolution of the porous matrix structure. Typical examples include quartz cementation in sandstones and smectite to illite transformation in shales [see, e.g., *Osborne and Swarbrick*, 1999; *Milliken,* 2004; *Taylor et al.*, 2010].

In this work we focus on quartz cementation phenomena, which are key in sandstones. Natural compaction processes in sedimentary basins take place on geological time scales, i.e., over millions of years (Ma), and the sediment thickness is typically of the order of kilometers

(km). Conversely, the critical physical and chemical processes take place at the pore scale and are commonly analyzed through laboratory experiments. A complete and rigorous model formulation which embodies the multiscale nature of the diagenetic processes is still not available and simplified effective models are usually adopted. The nature of the relationship between porosity and stresses is usually rendered through empirical models [e.g., *Schneider et al.*, 1994]. Issues related to quartz cementation, including the role of pressure and hydrocarbons in the precipitation/dissolution process as well as the proper identification of the source of silica, are still largely debated in the literature [e.g., *Milliken*, 2004; *Taylor et al.*, 2010]. Although inhibition of quartz cementation due to fluid overpressure has been observed at field scale [e.g., *Osborne and Swarbrick*, 1999] widely used quartz cementation models rely on the assumption that (*i*) quartz precipitation is a temperature-driven reaction-limiting factor [e.g., *Oelkers et al.*, 1996] and (*ii*) dissolution of grains and quartz precipitation occur at the same location, i.e. the source of quartz is local [e.g., *Walderhaug* 1994, 1996; *Lander and Walderhaug*, 1999]. Moreover, outputs of basin compaction models are affected by uncertainty, mainly due to the lack of knowledge on the appropriate conceptual and mathematical model and associated parameters. Since direct measurements of model parameters are typically scarce, parameter estimation can be performed by conditioning a given compaction model on measured state variables, such as temperature, heat flux, porosity, pressure and concentration profiles [*Zhao and Lerche*, 1993; *Tuncay and Ortoleva*, 2004; *Beha et al.*, 2008; *Huvaz et al.*, 2005; *Hurwitz et al.*, 2000].

Formaggia et al. [2013] recently presented a comprehensive simulation tool for the direct/forward modeling of sandstones compaction in the presence of quartz cementation. The model enables one to perform a global sensitivity analysis of the system states under uncertain

mechanical and geochemical model parameters and to obtain an efficient surrogate model of the compaction system. The surrogate model relies on a generalized Polynomial Chaos Expansion (gPCE) approximation of the system states [*Ghanem and Spanos*, 1991; *Xiu and Karniadakis*, 2002; *Le Maitre and Knio*, 2010] and is constructed through a sparse grid technique [*Babuska et al.*, 2010; *Nobile et al.* 2008; *Xiu and Hestaven*, 2005]. Due to its structure, the gPCE approximation of the model outputs can be evaluated at any location in space and time and for any combination of values of the uncertain parameters at a markedly reduced computational cost. As an additional benefit, mean, variance and (variance-based) Sobol sensitivity indices of target system states can be computed by simple algebraic manipulation of the gPCE coefficients. Sobol sensitivity indices [*Sobol*, 1991] also provide a direct quantitative measure of the influence of each uncertain parameter on the total variance of outputs of interest.

Here, we analyze the feasibility of estimating key parameters of a basin compaction model within an inverse Maximum Likelihood (ML) framework [e.g., *Carrera and Neuman*, 1986], where the full system model is replaced by its gPCE approximation. To this end, we set up an integrated methodology which combines (*i*) a forward numerical solver of compaction processes, (*ii*) a model reduction technique which allows approximating the model output variables through their gPCE, and (*iii*) a ML-based model inversion methodology to assimilate diverse types of information in a unique model calibration tool. The idea of accelerating the solution of inverse problems through the use of polynomial approximations has been already discussed in the subsurface hydrology literature. Examples of application of this technique include the analysis of (*i*) flow and transport in two- [*Müller et al.,* 2011] and three-dimensional [*Balakrishnan et al.*, 2003; *Lin and Tartakovsky,* 2009; *Laloy et al.* 2013] heterogeneous porous media, (*ii*) unsaturated [*Li et al.* 2009; *Sochala and Le Maitre*, 2013] and multi-phase [*Saad and*

Ghanem 2009; *Oladyshkin et al.* 2013] flow problems, and (*iii*) passive and reactive solute transport in column experiments [*Fajraoui et al.,* 2011, 2012; *Zhang et al.*, 2013; *Ciriello et al*. 2013]. Recent studies [e.g. *Lin and Tartakovsky*, 2009; *Liao and Zhang,* 2013] show that gPCE may be inaccurate in the presence of nonlinear relationships between input parameters and output variables. *Liao and Zhang* [2013] present an approach which allows overcoming this problem and apply their methodology to two-phase flow and solute transport taking place in one-dimensional heterogeneous and two-dimensional homogeneous systems.

A distinctive feature of our work is to demonstrate the reliability of gPCE-based approaches for the inverse modeling of basins whose evolution occurs over significantly large space-time scales and is governed by highly nonlinear equations. We also assess the impact of combining in a unique inverse modeling framework data of diverse nature which can be made available at a site. An additional original element of our study is the analysis of the way the ML inversion procedure can benefit from the adoption of anisotropic polynomial approximations (a-gPCE), in which the surrogate model is refined only with respect to selected parameters. The need for this refinement strategy is established according to an analysis of the nonlinearity of the input-output mapping, as quantified through the Sobol sensitivity indices.

The paper is organized as follows. Section 2 and 3 present an overview of the forward and inverse modeling techniques. Numerical results illustrating the application of the proposed methodologies are described in Section 4. Concluding remarks are then presented in Section 5.

2. BASIN COMPACTION MODELING

In this section, we briefly summarize the theoretical and numerical tools for the analysis of mechanical and geochemical compaction in a basin-scale model. Since evolutionary features of compacting sediments are mainly evolving along the vertical direction, one-dimensional

models of the type described in Section 2.1 are often employed and studied in the literature [e.g., *Lander and Walderhaug*, 1999; *Hurwitz et al.*, 2000; *Taylor et al.*, 2010]. In Section 2.2, we describe the numerical methodologies employed to derive the gPCE and a-gPCE models.

2.1 Forward basin compaction model

We consider a one-dimensional domain evolving with time, t, $z_{bot}(t)$ and $z_{top}(t)$ being the bottom and the top of the domain, respectively.

Mass conservation of fluid and solid phases in $\Omega(t)$ are respectively g $\Omega(t) = [z_{bot}(t), z_{top}(t)]$ overned by

$$\frac{\partial\left(\phi\rho^{l}\right)}{\partial t} + \frac{\partial\left(\phi u^{l}\rho^{l}\right)}{\partial z} = q^{l} \tag{1}$$

$$\frac{\partial\left[\left(1-\phi\right)\rho^{s}\right]}{\partial t} + \frac{\partial\left[\left(1-\phi\right)\rho^{s}u^{s}\right]}{\partial z} = q^{s} \tag{2}$$

where ϕ [-] is porosity, and u^i [m s^{-1}] and ρ^i [kg m^{-3}] respectively indicate the velocity and the density of i-phase (with $i = s$, l for the solid and fluid phase, respectively). The source terms q^i [kg m^{-3} s^{-1}] account for processes associated with fluid ($i = l$, e.g., water released during transformation of clay mineral) and solid ($i = s$, e.g., quartz precipitation) generation.

The Darcy flux, u^D [m s^{-1}], is given by

$$u^{D} = \phi\left(u^{l} - u^{s}\right) = \frac{K}{\mu^{l}}\left(\frac{\partial p}{\partial z} - \rho^{l} g\right) \tag{3}$$

where p [Pa] is pore pressure, μ^l [Pa s] is fluid dynamic viscosity, g [m s^{-2}] is gravity and K [m^2] is permeability. The latter is modeled as $K(\phi) = 10^{k_1\phi - k_2}$ [*Wangen*, 2010] where k_1 and k_2 are dimensionless fitting parameters usually estimated through laboratory experiments.

Variation of porosity, $d\phi$, is caused by mechanical compaction, $d\phi_M$, and by quartz precipitation, inducing an increase of quartz volumetric fraction, $d\phi_Q$, i.e., $d\phi = d\phi_M - d\phi_Q$. The rate of porosity change due to mechanical compaction is given by [e.g. *Schneider et al.*, 1994]

$$\frac{d\phi_M}{dt} = -\beta\left(\phi_0 - \phi_f\right)\exp\left(-\beta\sigma_C\right)\frac{d\sigma_C}{dt} \tag{4}$$

where

$$\frac{d\cdot}{dt} = \frac{\partial\cdot}{\partial t} + u^s\frac{\partial\cdot}{\partial z} \tag{5}$$

Here ϕ_0 is the initial porosity of the basin, ϕ_f is the minimum porosity value that can be attained by pure mechanical compaction, β [Pa^{-1}] is the porous medium (uniaxial) vertical compressibility and σ_C [Pa] is the effective stress, which is given by the difference between liquid pressure and total load.

Quartz precipitation is modeled as [e.g., *Walderhaug*, 1996]

$$\frac{d\phi_Q}{dt} = A\frac{M_Q}{\rho_Q}a_q 10^{b_q T}\ ; \qquad A = A_0\frac{\phi}{\phi_{act}};\ \ T > T_C \tag{6}$$

where ϕ_Q is quartz volumetric fraction, M_Q [kg mol^{-1}] and ρ_Q [kg m^{-3}] respectively are the molar mass and the density of quartz, A_0 [m^{-1}] and ϕ_{act} represent the specific surface and the actual porosity at the onset of quartz precipitation, and a_q [mol m^{-2} s^{-1}] and b_q [K^{-1}] are characteristic parameters of the system. The reaction represented by (6) takes place only if the temperature, *T,* is larger than a critical value T_C (usually assumed equal to 353 K). The main assumptions underlying equation (6) are (*i*) the source of quartz is local, (*ii*) the rate limiting factor is precipitation, (*iii*) the reactive process is temperature activated, (*iv*) the reaction rate does not depend on pressure, (*v*) a spherical growth of quartz grains takes place, and (*vi*) the effects of

clay coating are negligible. Albeit these assumptions may not be always verified [e.g., *Osborne and Swarbrick*, 1999] equation (6) is implemented in state-of-the-art basin evolution modeling tools [e.g., *Taylor et al.*, 2010].

The temperature evolution is modeled by

$$C_T \frac{dT}{dt} + \rho^l c^l u^D \frac{\partial T}{\partial z} - \frac{\partial}{\partial z}\left(K_T \frac{\partial T}{\partial z} \right) = 0; \qquad K_T = \lambda_l^{\phi} \left[\lambda_s \right]^{1-\phi} \tag{7}$$

where $C_T(\phi) = \phi\rho^l c^l + (1-\phi)\rho^s c^s$ is the effective thermal capacity of the medium, $K_T(\phi)$ [W m^{-1} K^{-1}] is the thermal conductivity, λ_s and λ_l are solid and fluid specific conductivities, c^l and c^s [J K^{-1} kg^{-1}] are the liquid and solid specific thermal capacities, respectively. Equation (7) models heat exchanges due to fluid advection and solid displacement as well as thermal diffusion. Note that K_T varies in space and time with ϕ, even in cases where λ_s and λ_l are constant. The nonlinear system of partial differential equations (1)-(7) is complemented by appropriate initial and boundary conditions, as detailed in Section 4.

In summary, the system (1)-(7) allows computing the full set of unknown state variables (fluid and solid phase velocities, pressure, temperature and porosity) describing the evolution of a one dimensional sedimentary basin in the presence of mechanical compaction and quartz precipitation. In the following, the system (1)-(7) is solved through the numerical approach proposed by *Formaggia et al.* [2013]. The scheme follows a Lagrangian perspective, where the computational mesh deforms under the effect of compaction and each cell follows the time evolution of a fixed portion of solid material. We refer to *Formaggia et al.* [2013] for additional details.

2.2 Model reduction technique and global sensitivity analysis

Inverse modeling (or history matching) typically requires solving the forward system model for several values of the unknown parameters. This step is usually computationally intensive. In the following we alleviate the computational burden by introducing a surrogate model of the full compaction system described by equations (1)-(7) in the form of a polynomial approximation.

We collect the N_p uncertain parameters, p_n, in a vector $\mathbf{p} \in \mathbb{R}^{N_p}$. Since no detailed information on geochemical compaction model parameters is typically available, each p_n is assumed to be described by a uniform distribution within the interval $\Gamma_n = \left[p_{n,min}, p_{n,max} \right]$, so that $\mathbf{p} \in \Gamma = \Gamma_1 \times \Gamma_2 \times ... \times \Gamma_{N_P}$. Any output of the full compaction model can thus be seen as a function $f(\mathbf{p}) : \Gamma \to \mathbb{R}$. The generalized Polynomial Chaos expansion [*Ghanem and Spanos*, 1991; *Xiu and Karniadakis,* 2002; L*e Maitre and Knio*, 2010] consists in approximating $f(\mathbf{p})$ by a linear combination of Q multivariate Legendre polynomials, $\psi_i(\mathbf{p})$, i.e.

$$f(\mathbf{p}) \approx \sum_{i=1}^{Q} \alpha_i \psi_i(\mathbf{p}) \tag{8}$$

Here α_i are real numbers called gPCE coefficients. Obviously, the accuracy of the approximation (8) increases with the number of polynomials Q considered in the gPCE. Legendre polynomials are used because they are orthonormal with respect to the uniform probability distribution assumed for p_n [*Xiu and Karniadakis,* 2002]. Note that the methodology does not rely on any other specific property of these polynomials. Thus, it can be applied for any distribution of p_n, upon substituting the Legendre polynomials with the appropriate family of orthonormal polynomials. The latter has been shown to exist for most of the distributions which are employed

to described commonly used random variables (such as uniform, Gaussian or exponential) with only a few exceptions [see e.g., *Ernst et al*., 2012].

The Q polynomials (8) are usually selected by enforcing some constraints on the degree of the gPCE with respect to each parameter p_n. It is convenient to use a multi-index (or vector) notation. Thus, instead of $\psi_i(\mathbf{p})$, with i scalar index, we introduce a vector $\mathbf{i}$ with N components $\mathbf{i}=[i_1,i_2,\ldots,i_N]$, and a multivariate Legendre polynomial, $\psi_{\mathbf{i}}(\mathbf{p})$, where the n-th component of the vector, i_n, specifies the polynomial degree of $\psi_{\mathbf{i}}(\mathbf{p})$ with respect to p_n. With this notation, (8) can be rewritten as

$$f(\mathbf{p}) \approx \sum_{\mathbf{i}\in\Lambda} \alpha_{\mathbf{i}} \psi_{\mathbf{i}}(\mathbf{p}), \tag{9}$$

where $\Lambda \subset \mathbb{N}^N$ is a user-defined set containing Q multi-indices, whose purpose is to specify which Legendre polynomials enter in the gPCE expansion. For a fixed Q, different choices for Λ are feasible. Common choices for Λ are

$$\Lambda = \{\mathbf{i}\in\mathbb{N}^N : \max_{n=1,2,\ldots,N} i_n \le w\}, \text{ for a given } w\in\mathbb{N}, \tag{10}$$

$$\Lambda = \{\mathbf{i}\in\mathbb{N}^N : \sum_{n=1}^{N} i_n \le w\}, \qquad \text{for a given } w\in\mathbb{N}, \tag{11}$$

$$\Lambda = \{\mathbf{i}\in\mathbb{N}^N : \sum_{n=1}^{N} \frac{i_n}{w_n} \le 1\}, \qquad \text{for a given set of values } w_1,w_2,\ldots,w_N \in \mathbb{N}. \tag{12}$$

In (10)-(11) w represents the maximum degree of the polynomial approximation with respect to each parameter p_n. The choice of Λ given by (10) (called "*tensor product gPCE*") is computationally impractical, as the number of the coefficients $\alpha_{\mathbf{i}}$ to be computed grows exponentially with *N*, according to the formula $Q=(w+1)^N$. The approach based on (11) (called

"*total degree gPCE*") markedly reduces this number, i.e., $Q=(N+w)!/\left(N!w!\right)$, while not compromising significantly the accuracy of the approximation [e.g., *Ghanem and Spanos*, 1991; *Le Maitre and Knio*, 2010]. However, the maximum polynomial degree of the resulting gPCE is the same with respect to each parameter, i.e., this formulation implicitly assumes that the same level of accuracy of the surrogate model is needed with respect to each p_n. Model (12) is more general and admits different maximum polynomial degrees, w_n, for each parameter p_n. In the following we adopt the strategies described by the sets (11) and (12), to construct the isotropic total degree gPCE and the anisotropic total degree gPCE, respectively. Hereinafter we refer to the former as "gPCE" and to the latter as "a-gPCE" for brevity.

The gPCE coefficients corresponding to the polynomials identified by the set Λ are defined by the following multidimensional integrals

$$\alpha_{\mathbf{i}}=\prod_{n=1}^{N}(p_{n,max}-p_{n,min})^{-1}\int_{\Gamma}f(\mathbf{p})\psi_{\mathbf{i}}(\mathbf{p})d\mathbf{p}\ , \tag{13}$$

These can be computed numerically by quadrature, least square approximation, or L^2 projection [*Ghanem and Spanos*, 1991; *Le Maitre and Knio*, 2010]. In this work, we consider a two-steps procedure originally proposed by *Formaggia et al* [2013], based on the so-called sparse-grid interpolation of $f(\mathbf{p})$ and summarized in Appendix A. We remark that this step requires the evaluation of $f(\mathbf{p})$, i.e., the solution of the full model, for several values of the uncertain parameters. An analysis of the computational costs involved in this procedure is provided in Section 4.

Once the coefficients $\alpha_{\mathbf{i}}$ have been computed, one notes that the gPCE expansion (9) is a linear combination of polynomials and can be evaluated very efficiently for any given $\mathbf{p}\in\Gamma$. Moreover, thanks to the orthonormality of the Legendre polynomials, simple algebraic

manipulations of the coefficients $\alpha_{\mathbf{i}}$ allow computing mean, $\mathbb{E}[f]$, and variance, $\mathbb{V}[f]$, of $f(\mathbf{p})$. Denoting by $\mathbf{0}$ the vector $\mathbf{0}=[0,0,\ldots,0]\in\mathbb{N}^N$, we have

$$\mathbb{E}[f]=\alpha_{\mathbf{0}},\qquad \mathbb{V}[f]=\sum_{\mathbf{i}\in\mathbb{N}^N}\alpha_{\mathbf{i}}^2-\alpha_{\mathbf{0}}^2\approx\sum_{\mathbf{i}\in\Lambda}\alpha_{\mathbf{i}}^2-\alpha_{\mathbf{0}}^2\ . \tag{14}$$

Equation (9) can be written as

$$f(\mathbf{p})\approx\alpha_{\mathbf{0}}\psi_{\mathbf{0}}+\sum_{n=1}^{N}\sum_{\mathbf{i}\in\mathcal{P}_n}\alpha_{\mathbf{i}}\psi_{\mathbf{i}}(\mathbf{p})+\sum_{n=1}^{N}\sum_{m=n}^{N}\sum_{\mathbf{i}\in\mathcal{P}_{n,m}}\alpha_{\mathbf{i}}\psi_{\mathbf{i}}(\mathbf{p})+\ldots, \tag{15}$$

where $\mathcal{P}_n\subset\Lambda$ denotes the subset of Λ containing the all of the multi-indices $\mathbf{i}$ such that only the n-th component is non-zero, $\mathcal{P}_{n,m}\subset\Lambda$ denotes the subset of Λ containing the all the multi-indices $\mathbf{i}$ such that only the n-th and the m-th components are non-zero and so on. The quantities

$$S_n=\sum_{\mathbf{i}\in\mathcal{P}_n}\frac{\alpha_{\mathbf{i}}^2}{\mathbb{V}[f]},\qquad S_{n,m}=\sum_{\mathbf{i}\in\mathcal{P}_{n,m}}\frac{\alpha_{\mathbf{i}}^2}{\mathbb{V}[f]}, \tag{16}$$

are approximations of the so-called Sobol indices that can be used to perform a global sensitivity analysis of the system outputs with respect to the input parameters [*Sobol*, 2001; *Sudret* 2007]. In particular, S_n is called the *principal* Sobol index of the n-th parameter, as it collects all contributions to the total variation of the $f(\mathbf{p})$ which are only due to the n-th parameter, p_n. Therefore it quantifies the actual need for an accurate estimate of p_n to reduce the uncertainty in the prediction of $f(\mathbf{p})$. The *total* Sobol index S_n^T is defined as

$$S_n^T=S_n+\sum_{k\neq n}S_{n,k}+\sum_{k,j\neq n}S_{k,j,n}+\ldots, \tag{17}$$

and includes S_n and all the joint terms where the n-th parameter appears. Note that a parameter could be associated with a small value of S_n and a large S_n^T, denoting that while p_n is not a relevant parameter per se, it becomes important when coupled with other parameters.

In light of the above discussion, we propose a Sobol-index based procedure to determine the coefficients $w_1,\ldots,w_N$ in (12). The basic idea is to rely, for each parameter, on Sobol indices to determine the number of (non- linear) polynomials to describe $f(\mathbf{p})$ by (9). To this purpose, we first build a coarse isotropic gPCE, using (11) with a small value of w (e.g., $w = 2$). We then compute the Sobol indices (16)-(17) and introduce the quantities

$$S_n^L = \frac{\alpha_{\mathbf{e}_n}^2}{\mathbb{V}[f]} \quad \text{and} \quad S_n^{NL} = S_n^T - S_n^L, \tag{18}$$

where $\mathbf{e}_n$ is the n-th canonical unit vector, i.e., $\mathbf{e}_n = [0,0,\ldots,0,1,0,\ldots,0] \in \mathbb{N}^N$, S_n^L is the Sobol index associated with the linear term including only parameter p_n, and S_n^{NL} represents the total contribution of nonlinear terms involving p_n, i.e., it indicates the degree of nonlinearity of the input-output mapping of $f(\mathbf{p})$ with respect to p_n. We set a priori a minimum and a maximum polynomial degree w_{min} and w_{max} depending on the envisioned complexity of $f(\mathbf{p})$. Then, we set w_n as

$$w_n = \max\left(\text{int}\left[w_{max}\frac{S_n^{NL}}{\max\left(S_n^{NL}\right)}\right], w_{min}\right). \tag{19}$$

In other words, we (*i*) estimate S_n^{NL} for each parameter, (*ii*) assign w_{max} and w_{min} to the two parameters respectively characterized by the maximum and minimum value of S_n^{NL}, and (*iii*) evaluate w_n for the remaining parameters by (19). Following this procedure, the non-linear impact of each parameter based on S_n^{NL} drives the choice of the polynomial order w_n.

As detailed above, the proposed methodology requires the construction of a preliminary coarse isotropic gPCE. Alternative procedures to assess the optimal set, Λ, of polynomials based on a-priori theoretical considerations or making used of ad-hoc algorithms have been proposed in the

literature [e.g., *Chkifa et al.*, 2013; *Beck et al.*, 2014]. However, these methods have been applied to analyze relatively simple phenomena governed by elliptic equations and their extension to complex processes, such as the problem we consider here, is not straightforward. In Section 4 we demonstrate the feasibility and accuracy of our proposed strategy.

3. INVERSE MODELING

In this section, we describe the Maximum Likelihood (ML) approach we adopt to obtain ML estimates, $\hat{\mathbf{p}}$, of $\mathbf{p}$ on the basis of porosity and/or temperature measurements. We set

$$\phi_i^* = \phi_i + \varepsilon_{\phi_i}^* \qquad i = 1,...,N_\phi \tag{20}$$

$$T_j^* = T_j + \varepsilon_{T_j}^* \qquad j = 1,...,N_T \tag{21}$$

where ϕ_i and T_j respectively are the (unknown) true values of ϕ and T at measurement points z_i and z_j at time t, ϕ_i^* and T_j^* are their (known) measured values affected by zero-mean measurement errors, $\varepsilon_{\phi_i}^*$ and $\varepsilon_{T_j}^*$, which are also unknown. In practical basin-scale problems the time t at which measurements becomes available usually coincides with the current observation time. Following the work of *Carrera and Neuman* [1986] we assume (*i*) the measurement errors $\varepsilon_{\phi_i}^*$ and $\varepsilon_{T_j}^*$ to be multivariate Gaussian, (*ii*) absence of spatial correlation and cross-correlation between measurement errors of ϕ and T, and (*iii*) the covariance matrix of measurements errors of ϕ ($\mathbf{C}_\phi$) and T ($\mathbf{C}_T$) to be given by

$$\mathbf{C}_\phi = \sigma_\phi^2 \mathbf{V}_\phi \qquad\qquad \mathbf{C}_T = \sigma_T^2 \mathbf{V}_T \tag{22}$$

where σ_ϕ^2, and σ_T^2 are typically unknown and can be estimated during the inversion. According to assumption (*ii*) $\mathbf{V}_\phi$ and $\mathbf{V}_T$ become diagonal matrices. In the examples presented in the

following we assume $\mathbf{V}_\phi = \mathbf{V}_T = \mathbf{I}$, i.e., the prior estimation errors of ϕ and T are constant in space.

The ML estimate $\hat{\mathbf{p}}$ is obtained by minimizing the negative log likelihood, *NLL*, criterion [e.g., *Carrera and Neuman*, 1986]. When direct measurements of $\mathbf{p}$ are not available, as in typical geochemical compaction settings, *NLL* is given by

$$NLL = \frac{J_\phi}{\sigma_\phi^2} + \frac{J_T}{\sigma_T^2} + N_\phi \ln \sigma_\phi^2 + N_T \ln \sigma_T^2 + N_D \ln(2\pi) \tag{23}$$

where $N_D = N_\phi + N_T$. The quantities J_ϕ and J_T respectively are the porosity and the temperature residual criteria (i.e., a weighted sum of the squared difference between simulated state variables and available observations) defined as

$$J_\phi = \left(\mathbf{\Phi} - \mathbf{\Phi}^*\right)' \mathbf{V}_\phi^{-1} \left(\mathbf{\Phi} - \mathbf{\Phi}^*\right); \tag{24}$$

$$J_T = \left(\mathbf{T} - \mathbf{T}^*\right)' \mathbf{V}_T^{-1} \left(\mathbf{T} - \mathbf{T}^*\right) \tag{25}$$

where superscript $'$ denotes transpose, $\mathbf{\Phi}^*$ and $\mathbf{T}^*$ are respectively vectors of porosity and temperature measurements, $\mathbf{\Phi}$ and $\mathbf{T}$ are vectors of porosity and temperature values evaluated according to the forward model (1)-(7) at measurement locations. Note that $\mathbf{\Phi}$ and $\mathbf{T}$ depend on the parameter vector $\mathbf{p}$. It is thus clear that minimization of *NLL* requires the solution of the system (1)-(7) for a (typically large) number of $\mathbf{p}$ values. This task can be extremely demanding in terms of CPU time, especially in the presence of strong model nonlinearities. Therefore, in this work we explore the feasibility of replacing (1)-(7) by the gPCE and a-gPCE approximations of $\mathbf{\Phi}$ and $\mathbf{T}$, which can be efficiently evaluated for any particular value of $\mathbf{p}$. For convenience of notation, in the following we use $\mathbf{\Phi}$ and $\mathbf{T}$ to refer to the Polynomial Chaos Expansion solutions.

Therefore, σ_ϕ^2, and σ_T^2 include both measurement and model errors, the latter being due to the use of the gPCE or a-gPCE approximations. In case σ_ϕ^2 and σ_T^2 be known, minimization of (23) is equivalent to minimizing the general least squares criterion

$$J = J_\phi + \lambda J_T \tag{26}$$

where $\lambda = \sigma_\phi^2 / \sigma_T^2$.

In the following, we consider the general case where σ_ϕ^2 and σ_T^2 (and therefore λ) are unknown *a priori*.

Riva et al. [2009, 2011] demonstrate that an accurate estimate of λ can be obtained on the basis of the Bayesian criterion *KIC* [*Kashyap*, 1982] defined as

$$KIC = NLL - N_P \ln 2\pi - \ln|\mathbf{Q}| \tag{27}$$

where $|\mathbf{Q}|$ is the Cramer-Rao lower bound approximation of the determinant of the covariance matrix of the estimation error, i.e.,

$$\mathbf{Q} = \sigma_\phi^2 \left(\mathbf{J}_\phi' \mathbf{V}_\phi^{-1} \mathbf{J}_\phi + \lambda \mathbf{J}_T' \mathbf{V}_T^{-1} \mathbf{J}_T \right)^{-1} \tag{28}$$

$\mathbf{J}_k$ (k = ϕ, T) being the Jacobian matrix whose entries are the derivatives of the output state variables (ϕ or T) with respect to the model parameters to be estimated. The ML estimates of σ_ϕ^2 and σ_T^2 are given by [*Carrera and Neuman*, 1986]

$$\hat{\sigma}_\phi^2 = \frac{J_{min}}{N_D} \qquad \hat{\sigma}_T^2 = \frac{\hat{\sigma}_\phi^2}{\lambda} \tag{29}$$

where J_{min} is the minimum value of J. Note that evaluation of $\mathbf{J}_k$ in (28) requires multiple solutions of the forward model. A key point of the Polynomial Chaos Expansion framework is that $\mathbf{J}_k$ can be obtained analytically, as ϕ and T are approximated by polynomial functions.

In summary, we propose to obtain ML estimates of the parameters characterizing a basin-scale system subject to mechanical and geochemical compaction according to the following steps:

1. Derivation of the gPCE surrogate model. This step requires solving the compaction problem (1)-(7) at each point of the sparse grid which is constructed in the parameter space.
2. Derivation of the a-gPCE surrogate model as described in Section 2.2.
3. Minimization of J for selected λ values. Minimization of (26) is performed through the Nelder-Mead simplex search method [*Nelder and Mead*, 1965; *Lagarias et al*., 1998]. In this work we repeat this step using six different initial parameters guesses, to avoid detecting local minima.
4. ML estimation of σ_ϕ^2 and σ_T^2 by (29) for each λ.
5. Selection of λ by minimizing (with respect to λ) *KIC* in (28).

The proposed methodology relies on minimal prior information on the parameters **p**, consistent with the assumed uniform probability density function (pdf) of model parameters. This choice is appropriate to characterize basins undergoing mechanical and geochemical compaction processes, where information on system parameters is usually not available due to large space-time scales characterizing the process.

4. ILLUSTRATIVE EXAMPLE

4.1 **Global sensitivity analysis and model reduction**

We illustrate the proposed methodology on a synthetic setting representative of basin compaction. This enables us to test the performance of the methodology described in Sections 2 and 3. The total sedimentation time we consider is 200 Ma and the sedimentation rate is fixed to 30 m Ma^{-1}. Temperature and pressure at the top of the basin are respectively set to 295 K and γ_{sea}

× h_{sea} (i.e., the hydrostatic pressure associated with the overlying sea depth, h_{sea}, γ_{sea} being the specific weight of seawater). For the purpose of our example we assume h_{sea} to be constant in time, thus disregarding possible erosion phenomena. As a consequence, the position of the top of the basin is constant with time. This, in turn, affects the temperature evolution, since a constant temperature is imposed at z_{top}. The bottom of the basin is assumed to be impermeable ($u^D = 0$) and subject to a given a geothermal gradient, G_T.

Formaggia et al. [2013] present a global sensitivity analysis of the system of equations (1)-(7). These authors consider uncertainty associated with (*i*) quartz cementation kinetic, a_q, (*ii*) relationship between porosity and permeability, (*iii*) sea paleobathimetry, h_{sea}, and (*iv*) vertical compressibility modulus, β. The (spatial) distributions of the resulting Sobol indices show that typical uncertainties on the three parameters β, a_q and h_{sea} bear the largest influence on porosity profiles, whereas temperature is mostly affected by a_q and h_{sea}. In this study, we additionally consider uncertainty in the geothermal gradient, G_T, which is expected to influence both temperature and porosity. The lower and upper bounds of the intervals of variability of the four uncertain parameters, $\left[p_{n,min}, p_{n,max} \right]$, are listed in Table 1. The selection of the width of these intervals has been based on typical values observed in real basins under compaction processes [*Walderhaug*, 1994; *Lander and Walderhaug*, 1999; *Wangen*, 2010]. The remaining parameters are assumed constant. We set: k_1 = 14.15, k_2 = 16.94 [*Wangen*, 2010], $\rho^l = 999$ kg m^{-3}, $\rho^s = 2323$ kg m^{-3}, $q^l = 0$, i.e., no internal source of liquid phase is considered. The limiting porosity for mechanical compaction is imposed to ϕ_f = 0.28 [*Wangen*, 2010]. Characteristic parameters for quartz cementation are set to M_Q = 6.001 kg mol^{-1}, ρ_Q = 2650 kg m^{-3}, ϕ_{act} = 0.3, T_C = 353 K, $A_0 = 10^4$ m^{-1}, b_q = 273.172 K^{-1} [*Walderhaug*, 1994; *Lander and Walderhaug*, 1999]. The thickness of the basin at the initial simulation time is equal to 500 m and initial spatial

distribution of porosity is assigned through standard Athy's law [e.g., *Schneider et al.*, 1994] to include mechanical compaction.

Figure 1 depicts the vertical profiles of the average porosity and temperature at the final deposition time evaluated from the first of (14). These results are obtained upon sampling the selected uncertain parameters within the intervals listed in Table 1 and using a *total degree* gPCE (see (11)) at level $w = 3$. Uncertainty intervals of width equal to ± one standard deviation (evaluated as the square root of the second of (14)) around the mean are also shown. Figure 2 depicts the vertical distribution of the Sobol indices associated with the profiles of Figure 1. Here, gray and black shaded areas indicate the linear Sobol coefficients S_n^L (18) and the principal Sobol indices S_n (16), respectively, whereas the dashed curves correspond to the total Sobol indices S_n^T (17). Figure 1a reveals that the mean porosity reduces with a seemingly exponential trend as z decreases until $z \cong -2000$ m. This behavior is consistent with equation (4) and is due to mechanical compaction, being strongly influenced by β and h_{sea}, as shown in Figure 2a. The dependence of porosity on β and h_{sea} is almost linear, i.e., $S_n^T \approx S_n^L$. Quartz cementation starts at about $z \approx -2000$ m where the Sobol indices related to a_q and G_T increase. The porosity rapidly decreases for $z < -2000$ m, where its variance tends to increase, as shown by Figure 1a. Due to geochemical compaction we observe here porosity values which are smaller than ϕ_f. In this region, the porosity depends nonlinearly on the parameters a_q and G_T (Figure 2a). Note also that at deep locations we observe that $S_{a_q}^T > S_{a_q}$ and $S_{G_T}^T > S_{G_T}$, implying that the mixed terms including a_q and G_T are relevant in the gPCE approximation of porosity.

Mean temperature (Figure 1b) increases rapidly with depth until $z \approx -2000$ m. The temperature gradient decreases when quartz cementation becomes relevant ($z > 2000$ m). This

behavior is associated with the decrease of accessible pore space, which influences the thermal conductivity of the medium at large burial depths. Figure 2b reveals that the temperature distribution is highly influenced by G_T and h_{sea}, as these parameters are strictly related to the boundary conditions of the thermal problem. On the other hand, a_q and especially β have only a reduced influence. The dependence of temperature on all the parameters is almost linear at each depth.

Since nonlinear dependence has been observed between ϕ and the parameters a_q and G_T, in the following we derive an appropriate a-gPCE for ϕ according to the methodology described in Section 2. The nonlinear term S_n^{NL} (with $n = a_q, G_T$) depicted in Figure 2a is represented by the difference between S_n^T and S_n^L, as described by (18). Since the indices S_n^{NL} vary with z, we consider the following average value as a global indicator of nonlinearity

$$\overline{S}_n^{NL} = \frac{1}{z_{max} - z_{min}} \int_{z_{min}}^{z_{max}} S_n^{NL} dz \tag{30}$$

where z_{min} and z_{max} are the minimum and maximum depths associated with locations at which data are available. For our example, we obtain $\overline{S}_{G_T}^{NL} = 0.180$ and $\overline{S}_{a_q}^{NL} = 0.117$. Since $\overline{S}_{G_T}^{NL} > \overline{S}_{a_q}^{NL}$, the a-gPCE is computed by setting $w_{G_T} = w_{max} = 6$. Nonlinear effects due to h_{sea} and β are negligible, and therefore we set $w_{hsea} = w_\beta = w_{min} = 2$. Following the criterion (19), we derive $w_{a_q} = 4$. When the a-gPCE, is considered the spatial distributions of the Sobol indices are very similar to those displayed in Figure 2a, the only difference being that small oscillations appearing in Figure 2a for $z < -3000$ m are smoothed out (details not shown).

We note that while gPCE approximations might deteriorate with time (e.g., *Gerritsma et al.*, 2010), *Formaggia et al.* [2013] verified the accuracy of gPCE to describe the evolution of

porosity and temperature within a problem setting similar to the one we consider in this work. Additional evidences of the reliability of the derived gPCE and a-gPCE approximations for this test case are provided in Appendix B.

4.2 Inversion modeling and results

In the following, we present the results of the proposed model inversion procedure. We first present the selected datasets. Then, we investigate the impact of (*i*) the order *w* of the gPCE approximation, (*ii*) the use of the a-gPCE procedure, and (*iii*) the quality and type of calibration data, on the model inversion results. The impact of the available calibration data on the estimate of compaction-driven flow history is also quantified.

4.2.1 Calibration datasets

The reference porosity $\mathbf{\Phi}_{true}$ and temperature $\mathbf{T}_{true}$ fields have been generated by solving (1)-(7) with the values $p_n = p_{n,true}$ listed in Table 1. The vertical profiles $\mathbf{\Phi}_{true}$ and $\mathbf{T}_{true}$ computed at the final simulation time (t = 200 Ma) are shown in Figure 3. We sample $\mathbf{\Phi}_{true}$ and $\mathbf{T}_{true}$ at 41 equally spaced locations along the z-axis to obtain the information employed in the inversion procedure. In order to simulate measurements errors, the calibration data $\mathbf{\Phi}^*$ and $\mathbf{T}^*$ in (24)-(25) are obtained by superimposing to $\mathbf{\Phi}_{true}$ and $\mathbf{T}_{true}$ the white Gaussian noises having standard deviations respectively equal to σ_ϕ and σ_T, whose values are listed in Table 2. Note that when $\sigma_f = 0$ (with $f = \phi$ and/or T) the only source of error in the calibration data is due to the gPCE or a-gPCE approximation of porosity and temperature profiles. The values of σ_f have been selected to allow the ratios $\sigma_\phi / \Delta\phi_{true}$ and $\sigma_T / \Delta T_{true}$ to vary between 1% and 15% (see Table 2), where $\Delta\phi_{true}$ and ΔT_{true} are the widths of the intervals comprised between the minimum and maximum values displayed by $\mathbf{\Phi}_{true}$ and $\mathbf{T}_{true}$ along z. The datasets $\mathbf{\Phi}_1^*$, $\mathbf{\Phi}_3^*$, $\mathbf{\Phi}_5^*$, $\mathbf{T}_1^*$, $\mathbf{T}_3^*$, $\mathbf{T}_5^*$

corresponding to the minimum, intermediate and maximum values of σ_f are also depicted in Figure 3. To summarize, in the following we consider 17 calibration datasets: (*a*) one dataset comprising only unperturbed porosity values $\mathbf{\Phi}_0^*$; (*b*) one dataset comprising only unperturbed temperature values $\mathbf{T}_0^*$; (*c*) five datasets including only perturbed porosity values $\mathbf{\Phi}_i^*$ with i = 1,..5; (*d*) five datasets including only perturbed temperature values $\mathbf{T}_i^*$ with i = 1,..,5; and (*e*) five datasets comprising perturbed values of both porosity and temperature ($\mathbf{\Phi}_i^*$, $\mathbf{T}_i^*$) with i = 1,..,5.

4.2.2 Analysis of gPCE and a-gPCE approximations in the inversion procedure

Here we assess the impact of the choice of the Polynomial Chaos Expansion model on the inversion results. We start by assuming that only unperturbed porosity, $\mathbf{\Phi}_0^*$, or temperature, $\mathbf{T}_0^*$, data are available and compare outputs of the inversion procedures obtained with various orders w of gPCE and a-gPCE approximations. With reference to the isotropic setting, we use the total degree gPCE at three levels, i.e., w = 3, 4, 5. Table 3 lists the values of *NLL* and *KIC* evaluated at the end of the inversion procedure. These results show that the three isotropic gPCE surrogate models renders very similar minima of *NLL* and *KIC* when $\mathbf{\Phi}_0^*$ is employed. These minima then decrease with w when $\mathbf{T}_0^*$ is employed. The a-gPCE enables us to obtain significantly decreased values of *NLL* and *KIC*. The best surrogate model in terms of these two criteria appears to be given by a-gPCE.

The accuracy of each set of parameter estimates is quantify by the ratios $\eta_{p_n} = \hat{p}_n / p_{n,true}$ listed in Table 3. In general all quantities η_{p_n} converge to unity as w increases. The anisotropic sparse grid renders results of the same (or improved) quality as those provided by gPCE with w = 5, while markedly decreasing the CPU time, as also detailed in Table 3.

To assess the performance of the methodology in the presence of a perturbed datasets, Table 4 lists η_{p_n} and the ratio between ML estimate of σ_ϕ, $\hat{\sigma}_\phi$, and its true value evaluated when $\mathbf{\Phi}_3^*$ (see Table 2) is employed. Table 4 reports the outcomes obtained through gPCE with w = 3, 4, 5, a-gPCE and the full model (FM) (1)-(7). CPU times associated with each model inversion strategy are summarized in Figure 4. Numerical computations have been performed on 3.2 GHz Intel i7 processors. As noted earlier, the accuracy of parameter estimates tends to increase with w (see Table 4). Figure 4 illustrates that the CPU time increases by one order of magnitude moving from w = 3 to w = 5. On the other hand, the results of Table 4 show that the a-gPCE yields results of accuracy comparable to that obtained with gPCE and w = 5 or with the full model, but requires a CPU time which is similar to that needed by gPCE with w = 3 as shown in Figure 4. Figure 4 also illustrates in graphical form the time associated with the construction of the polynomial chaos approximations and the one required by the inversion step. Note that the CPU time needed to complete the inversion step with a-gPCE and with the full model differ by more than two orders of magnitude. This observation is relevant since the surrogate model can be constructed only once and can then be exploited to perform several model calibrations using diverse (in terms of quality and quantity) datasets. This result has important consequences when porosity and temperature data are both available, as multiple model calibrations are needed for the estimation of λ, as detailed in Section 3.

From the analyses performed in this section, we conclude that the anisotropic sparse grid technique is conducive to a marked reduction of the computational cost, while maintaining the same level of accuracy of the full model. Therefore, in the following subsections we perform the inversion procedure upon relying only on the a-gPCE.

4.2.3 Assessment of calibration datasets

Here we consider the effect of (*i*) measurement errors and (*ii*) joint use of porosity and temperature measurements on the inversion outcomes.

Figure 5 shows the variation of the coefficients η_{p_n} as function of the type of calibration data and of the standard deviations of the measurement errors adopted during the inversion. The left column shows the results obtained considering only porosity data ($\mathbf{\Phi}_i^*$, with i = 1,…5), the central column shows the corresponding results derived with temperature data only ($\mathbf{T}_i^*$,with i = 1,...5), and the right column depicts the results obtained on the basis of porosity and temperature information ($\mathbf{\Phi}_i^*, \mathbf{T}_i^*$, with i = 1,...5). The joint calibration datasets are characterized by a constant ratio $\sigma_\phi / \sigma_T = 0.004$, which renders a constant value of λ, $\lambda = \sigma_\phi^2 / \sigma_T^2 = 1.6 \times 10^{-5}$. According to the procedure illustrated in Section 3, we minimize the objective function (26) for selected values of λ comprised in the interval [10^{-7}, 1]. Figure 5 also depicts the uncertainty intervals of width $\pm\ \hat{\sigma}_{p_n} / p_{n,true}$, where $\hat{\sigma}_{p_n}$ is given by the square root of the diagonal terms of (29). Black dots in Figure 5 indicate cases where $\hat{p}_i$ lie outside the range $\left[p_{n,min}, p_{n,max} \right]$ defined in Table 1 and a-gPCE approximations of temperature and porosity are not valid. Gray circles identify the cases where $\hat{p}_n + \hat{\sigma}_{p_n} > p_{n,max}$ or $\hat{p}_n - \hat{\sigma}_{p_n} < p_{n,\min}$. Figure 5 shows that estimates of G_T and h_{sea} are generally accurate and affected by reduced uncertainty in the presence of temperature or porosity measurements. On the other hand, estimates of a_q and β are more accurate upon relying on porosity rather than on temperature data (compare Figures 5a, d against Figures 5b, e). This is consistent with the Sobol indices analysis (Figure 2b), which shows that the effect of a_q and β on the temperature profile is almost negligible. Figure 5d hilights that estimates $\hat{a}_q$ are characterized by relevant uncertainty when only porosity data are available and

their measurement error is not negligible (i.e., $\sigma_\phi / \Delta\phi_{true} \geq 4\%$). The joint use of porosity and temperature measurements clearly improves the accuracy of all estimates (see right column of Figure 5) and significantly reduces the related uncertainty bounds. Results of Figure 5 are complemented by Table 5, where we list estimates of the porosity and/or temperature standard deviations $\hat{\sigma}_f$ ($f = \phi, T$) and of the regularization weight, $\hat{\lambda}$, provided by the analysis of all datasets. The estimated and true measurement error standard deviations are quite close, $\hat{\sigma}_f$ slightly underestimating the corresponding true values listed in Table 1 with a maximum discrepancy of about 20%. Estimates $\hat{\lambda}$ range between 1.2×10^{-5} and 2.4×10^{-5} and are also very similar to the true value (1.6×10^{-5}).

4.2.4 Analysis of compaction-driven flow

During the compaction period, fluid in a sedimentary basin flows from the underlying formations towards shallower and more permeable regions. This phenomenon is called compaction-driven upward flow and its prediction is key in practical environmental applications to analyze transport processes at shallow locations [e.g, *Hurwitz et al.*, 2000; *Bonnesen et al.*, 2009].

Here, we assess the propagation of the uncertainty associated with the parameters estimated in Section 4.2.3 on compaction-driven flow history. As described in Section 2, the Darcy flux, u^D, is directly linked to the porosity according to (3). Figure 6 shows the time evolution of u^D_{true}, i.e., the Darcy flux computed at a shallow location ($z = -650$ m) by (1)-(7) and imposing the true parameter values listed in Table 1. Qualitatively similar results have also been obtained at different values of z in the shallow zone (i.e., for z of the order of few hundred meters or less). Note that u^D_{true} increases in time and reaches approximately 1.5 cm y^{-1} for $t > 150$

Ma. This value is close to experimental data observed in previous works [e.g., *Hurwitz et al*, 2000]. Figure 6 also depicts the a-gPCE approximation of u^D calculated using the ML estimates of p_n obtained with the datasets $\mathbf{\Phi}_2^*$, $\hat{p}_n\left(\mathbf{\Phi}_2^*\right)$, (Figure 6a) and $\left(\mathbf{\Phi}_2^*, \mathbf{T}_2\right)$, $\hat{p}_n\left(\mathbf{\Phi}_2^*, \mathbf{T}_2\right)$, (Figure 6b). These datasets have been selected for illustration purposes as they are characterized by intermediate values of measurement error variances. Both predictions based on $\hat{p}_n\left(\mathbf{\Phi}_2^*\right)$ or $\hat{p}_n\left(\mathbf{\Phi}_2^*, \mathbf{T}_2\right)$ are able to accurately reproduce u_{true}^D. Finally, we perform a Monte Carlo analysis based on 5000 realizations derived on the basis of the a-gPCE model by sampling the model parameters from a Gaussian distribution with mean equal to $\hat{p}_n$ and standard deviation given by $\hat{\sigma}_{p_n}$. Monte Carlo simulations of u^D are depicted in Figure 6 for both cases. The uncertainty in the prediction of the Darcy flux is greatly reduced when temperature and porosity data are jointly used.

5. CONCLUSIONS

We present a methodology for the inversion of a model describing basin-scale mechanical and geochemical compaction processes. Our strategy is based on the use of reduced complexity models of the system and is framed within a Maximum Likelihood (ML) context. The anisotropic Polynomial Chaos Expansion (a-gPCE) of porosity and temperature distributions is derived upon relying on a two-steps methodology based on Sobol sensitivity indices. We illustrate the proposed technique in the context of a one-dimensional synthetic test case when compaction occurs due to the effects of mechanical stresses and precipitation of quartz. Our work leads to the following major conclusions.

1. The Sobol-index based methodology implemented to compute the a-gPCE provides a simple and effective criterion to improve the accuracy of the resulting surrogate model. In

our illustrative example we show that a-gPCE allows increasing the accuracy of the parameter estimates while maintaining a reduced computational cost in comparison with isotropic gPCE.

2. Vertical profiles of porosity are typically employed to characterize compaction processes in sedimentary basins. Our results show that model inversion performed with only porosity data renders acceptable estimates of the key model parameters. A large uncertainty prediction is associated with the quartz cementation rate, a_q. This result suggests that an accurate estimation of parameters linked to geochemical processes may become a critical factor, when relying only on porosity data.
3. Relying only on temperature data does not lead to acceptable estimates of a_q and of the mechanical compaction modulus, β. This result is consistent with the behavior of the Sobol indices which show that a_q and β do not have a strong influence on the thermal problem. Otherwise, when porosity and temperature measurements are jointly considered all parameter estimates are close to their true counterparts and their estimation uncertainty is considerably reduced. This result highlights that, in practical applications, there is the urge to monitor not only the porosity (as usually performed) but also the temperature vertical profiles along boreholes.

The scheme adopted in this work relies on a conceptual model according to which the basin is mainly composed of a single geomaterial. Future extensions of this study include the analysis of (a) compaction processes in heterogeneous systems, which originate for example by the alternating deposition of sandstone and clay layers, (b) different geochemical compaction phenomena (such as smectite to illite transformation), and (c) the benefit of using additional

information (e.g., pressure distribution) for an accurate characterization of the system. These studies are critical to guide the experimental activity in field test cases.

ACKNOWLEDGMENT

The authors are grateful for the partial financial support from Eni SpA. L. Tamellini has received support by the Italian grant FIRB-IDEAS (Project n. RBID08223Z) "Advanced numerical techniques for uncertainty quantification in engineering and life science problems". The data used to produce the results of this paper are available for free upon request to the corresponding author.

APPENDIX A: COMPUTATION OF THE gPCE AND a-gPCE

In this Appendix we provide some details on the procedure employed to compute the coefficients of the gPCE and a-gPCE described in Section 2. We employ a two-step procedure: first we compute an intermediate approximation of $f(\mathbf{p})$, namely the "sparse grid interpolant" of $f(\mathbf{p})$, and then we convert such interpolant into an equivalent polynomial chaos approximation.

For a one-dimensional function $g(p_n):\Gamma_n \to \mathbb{N}$ and for an integer number j_n denoting the approximation level, we consider a set of j_n points over Γ_n, $p_n^1, p_n^2, \ldots, p_n^{j_n}$. We denote by $\mathcal{U}_n^{j_n}[g]$ the unique polynomial of degree $j_n - 1$ that interpolates the function g at $p_n^1, p_n^2, \ldots, p_n^{j_n}$, i.e., $\mathcal{U}_n^{j_n}[g](p_n^k) = g(p_n^k)$ for $k = 1, 2, \ldots, j_n$. If the set of j_n points covers appropriately Γ_n and if g is a regular function, the accuracy of $\mathcal{U}_n^{j_n}[g]$ increases with j_n.

Similarly, for the multidimensional function $f(\mathbf{p})$ and for a multi-index vector $\mathbf{j}$ denoting the approximation level along each direction, we consider the Cartesian (or tensorial) grid over Γ composed by $j_1 \times j_2 \ldots \times j_n$ interpolation points (i.e., j_n points along each direction p_n), which we term $\mathcal{H}_\mathbf{j}$. We then denote by $\mathcal{M}^\mathbf{j}[f]$ the unique multivariate polynomial of degree $j_n - 1$ along

each direction p_n interpolating $f(\mathbf{p})$ at each point of $\mathcal{H}_\mathbf{j}$. Note that the polynomial $\mathcal{M}^\mathbf{j}[f]$ can be expressed as a linear combination of Legendre polynomials with degree not exceeding $j_n - 1$ along each direction p_n

$$\mathcal{M}^\mathbf{j}[f] = \sum_{\mathbf{i}\in\Lambda} \alpha_\mathbf{i} \psi_\mathbf{i}(\mathbf{p}), \tag{A1}$$

where $\Lambda = \{\mathbf{i} \in \mathbb{N}^N : i_n < j_n - 1\}$ and the coefficients $\alpha_\mathbf{i}$ can be computed by imposing that the polynomial $\mathcal{M}^\mathbf{j}[f]$ is equal to $f(\mathbf{p})$ when evaluated at every point $\mathbf{p}_k$ of the grid $\mathcal{H}_\mathbf{j}$, i.e., solving the linear system

$$\sum_{\mathbf{i}\in\Lambda} \alpha_\mathbf{i} \psi_\mathbf{i}(\mathbf{p}_k) = f(\mathbf{p}_k), \quad \forall \mathbf{p}_k \in \mathcal{H}_\mathbf{j}. \tag{A2}$$

The number of points required to build $\mathcal{M}^\mathbf{j}[f]$ grows exponentially with the number of parameters N_p. Therefore, increasing the number of interpolation points equally in all directions is not computationally convenient. The sparse grid interpolant, f_{SG}, circumvents this problem by approximating $f(\mathbf{p})$ by a linear combination of several small multivariate interpolant polynomials, which are built according to the *sparsification* principle, i.e., whenever high accuracy is reached along a given direction, the accuracy in the other directions should be kept at a minimum. This principle is formulated as

$$f(\mathbf{p}) \approx \sum_{\mathbf{j}\in\mathcal{I}} c_\mathbf{j} \mathcal{M}^\mathbf{j}[f](\mathbf{p}) = f_{SG}^{\mathcal{I}}(\mathbf{p}) \tag{A3}$$

where $c_\mathbf{j}$ are suitable coefficients [see, e.g., *Formaggia et al.*, 2013] and $\mathcal{I}$ is a set of multi-indices that drives the *sparsification* procedure, i.e., it specifies which multivariate interpolant polynomial $\mathcal{M}^\mathbf{j}[f](\mathbf{p})$ should be included in the sparse grid interpolant. Each $\mathcal{M}^\mathbf{j}[f](\mathbf{p})$ can be expressed as a combination of multivariate Legendre polynomials. Therefore, converting the sparse grid approximation $f_{SG}^{\mathcal{I}}(\mathbf{p})$ into its equivalent gPCE form only requires solving as many

linear system (A3) as the number of interpolant polynomials composing $f_{SG}^{\mathcal{I}}(\mathbf{p})$ and then collecting in a single term all the Legendre polynomials $\psi_{\mathbf{i}}(\mathbf{p})$ appearing in more than one interpolant $\mathcal{M}^{\mathbf{j}}[f](\mathbf{p})$.

Different sparse grids interpolants can be obtained upon varying $\mathcal{I}$. A final gPCE satisfying (12) can be derived setting [*Bäck et al.*, 2011]

$$\mathcal{I}=\left\{\mathbf{j}\in\mathbb{N}^N:\sum_{n=1}^{N}\frac{j_n-1}{w_n}\leq 1\right\} \tag{A4}$$

Figure A1 depicts an example of a sparse grid construction. Figure A2 shows three different interpolants: (*i*) a multivariate interpolant polynomial $\mathcal{M}^{\mathbf{j}}[f]$ with 17 points along each direction (tensor grid, Figure A2a), (*ii*) a sparse grid built according to (A4) with $w_i = 4$ ($i = 1, 2$) (isotropic sparse grid, Figure A2b), and (*iii*) a sparse grid generated by (A4) with $w_1 = 4$ and $w_2 = 2$ (anisotropic sparse grid, Figure A2c).

APPENDIX B: NUMERICAL ASSESSMENT OF THE QUALITY OF gPCE AND a-gPCE

Here, we assess the accuracy of the gPCE and a-gPCE models described in Section 4. To this end, we randomly select 500 sets of parameters within the parameters space Γ (see Table 1) and simulate the resulting temperature and porosity profiles through (*i*) the full system model described by (1)-(7), (*ii*) gPCE of order $w = 3$ and (*iii*) a-gPCE. Figure B1 are scatterplots of gPCE and a-gPCE solutions of porosity (Figure B1a-b) and temperature (Figure B1c-d) versus full model outcomes at locations corresponding to the measurement points (see Figure 3) and at the final simulation time. Both surrogate models (gPCE and a-gPCE) accurately reproduce the temperature values obtained by the full compaction model as demonstrated by Figure A3c-d. The a-gPCE approximation of porosity is markedly closer to the full model counterpart than the

gPCE, especially in the intermediate range $0.15 < \phi < 0.4$ (see Figure A3a-b). The mean squared error (MSE) between the full model and the gPCE and a-gPCE approximations of ϕ is 5.63×10^{-5} and 2.31×10^{-5}, respectively.

REFERENCES

Babuska, I., F. Nobile, and R. Tempone (2010), A stochastic collocation method for elliptic partial differential equations with random input data, SIAM Rev., 52(2), 317-355, 10.1137/100786356.

Bäck, J., F. Nobile, L. Tamellini, and R. Tempone (2011), Stochastic Spectral Galerkin and Collocation methods for PDEs with random coefficients: a numerical comparison, in Spectral and High Order Methods for Partial Differential Equations, Lecture Notes in Computational Science and Engineering, 76, edited by. J. Hestaven and E. Ronquist, pp. 43-62, Springer, doi:10.1007/978-3-642-15337-2_3.

Balakrishnan, S., A. Roy, M. G. Ierapetritou, G. P. Flach, and P. G. Georgopoulos (2003), Uncertainty reduction and characterization for complex environmental fate and transport models: an empirical Bayesian framework incorporating the stochastic response surface method, Wat. Resour. Res., 39(12), SBH81-SBH813, doi:10.1029/2002WR001810.

Beck, J., F. Nobile, L. Tamellini, and R. Tempone (2014), A quasi-optimal sparse grids procedure for groundwater flows, in Spectral and High Order Methods for Partial Differential Equations, Lecture Notes in Computational Science and Engineering, 95, , edited by M. Azaiez et al., pp 1-16, Springer, doi:10.1007/978-3-319-01601-6_1.

Beha, A., R. O .Thomsen, and R. Littke (2008), A rapid method of quantifying the resolution limits of heat-flow estimates in basin models, J Petrol. Geol., 31, 167-178, doi: 10.1111/j.1747-5457.2008.00414.x.

Bonnesen, E.P., F. Larsen, T. O. Sonnenborg, K. Klitten and L. Stemmerik (2009), Deep saltwater in Chalk of North-West Europe: origin, interface characteristics and development over geological time, Hydrogeol. J., 17, 1643-63, doi: 10.1007/s10040-009-0456-9.

Carrera, J., and S. P. Neuman (1986), Estimation of aquifer parameters under transient and steady state conditions: 1. Maximum likelihood method incorporating prior information, Wat. Resour. Res., 22 (2),199-210.

Chkifa, A., A. Cohen, R. Devore, and C. Schwab (2013), Sparse adaptive Taylor approximation algorithms for parametric and stochastic elliptic PDEs, ESAIM: Math. Model. Num., 47(1), 253–280, doi:10.1051/m2an/2012027.

Ciriello, V., A. Guadagnini, V. Di Federico, Y. Edery, and B. Berkowitz (2013), Comparative analysis of formulations for conservative transport in porous media through sensitivity-based parameter calibration, Water Resour. Res., 49(9), 5206-5220, doi: 10.1002/wrcr.20395.

Ernst, O., A. Mugler, H. J. Starkloff, and E. Ullmann (2012), On the convergence of generalized polynomial chaos expansions, ESAIM: Mathematical Modelling and Numerical Analysis 46 (2012), doi:10.1051/m2an/2011045.

Fajraoui, N., F. Ramasomanana, A. Younes, T. Mara, P. Ackerer, and A. Guadagnini (2011), Use of global sensitivity analysis and polynomial chaos expansion for interpretation of non reactive transport experiments in laboratory scale porous media, Water Resour. Res, 47(2), W02521, doi:10.1029/2010WR009639.

Fajraoui, N., T. A. Mara, A. Younes, and R. Bouhlila (2012), Reactive transport parameter estimation and global sensitivity analysis using sparse Polynomial Chaos Expansion, Water, Air, & Soil Pollution, 223(7), 4183-4197, doi: 10.1007/s11270-012-1183-8.

Formaggia L., A. Guadagnini, I. Imperiali, V. Lever, G. M. Porta, M. Riva, A. Scotti, and L. Tamellini (2013), Global sensitivity analysis through polynomial chaos expansion of a basin-scale geochemical compaction model, Computat. Geosci., 17(1), 25-42, doi: 10.1007/s10596-012-9311-5.

Gambolati, G., G. Ricceri, W. Bertoni, G. Brighenti, and E. Vuillermin (1991), Mathematical simulations of the subsidence of Ravenna, Water Resour. Res., 27(11), 2899-2918, doi: 10.1029/91WR01567.

Gambolati, G., P. Teatini, D. Bau and M. Ferronato (2000), Importance of poroelastic coupling in dynamically active aquifers of the Po river basin, Italy, Water Resour. Res., 36(9), 2443-2459, doi: 10.1029/2000WR900127.

Gerritsma, M., J. B. van der Steen, P. Vos and G. Karniakidis (2010), Time-dependent generalized polynomial chaos, J. Comput. Phys., 229(22), 8333-63, doi:10.1016/j.jcp.2010.07.020.

Ghanem, R. G., and P. D. Spanos (1991) Stochastic finite elements: a spectral approach, Springer-Verlag, New York.

Hoffmann, J., D. L. Galloway, and H. A. Zebker (2003), Inverse modeling of interbed storage parameters using land subsidence observations, Antelope Valley, California, Water Resour. Res., 39(2), 1031, doi:10.1029/2001WR001252.

Hurwitz, S., V. Lyakhovsky, and H. Gvirtzman (2000), Transient salt transport modelling of shallow brine beneath a freshwater lake, the sea of Galilee, Israel, Water Resour. Res., 36(1), 101-107, doi:10.1029/1999WR900292.

Huvaz, O., R. O. Thomsen, and S. Noeth (2005), A method for analyzing geothermal gradient histories using the statistical assessment of uncertainties in maturity models, J. Petrol. Geol., 38, 107-118, doi:10.1111/j.1747-5457.2005.tb00075.x.

Jiao, J. J., and C. Zheng, (1998), Abnormal fluid pressures caused by deposition and erosion of sedimentary basins, J. Hydrol., 204, 124-137, doi:10.1016/S0022-1694(97)00115-7.

Kashyap, R. L., (1982), Optimal choice of AR and MA parts in autoregressive moving average models, IEEE T. Pattern. Anal. 4(2):99–104.

Kreitler, C. H., (1989), Hydrogeology of sedimentary basins, J. Hydrol., 106, 29-53, doi:10.1016/0022-1694(89)90165-0.

Lagarias, J. C., J. A. Reeds, M. H. Wright, and P. E. Wright (1998), Convergence properties of the Nelder-Mead simplex method in low dimensions, SIAM J. of Optimiz., 9(1), 112-147, doi: 10.1137/S1052623496303470.

Laloy, E., B. Rogiers, J.A. Vrugt, D. Mallants, and D. Jacques (2013), Efficient posterior exploration of a high-dimensional groundwater model from two-stage MCMC simulation and polynomial chaos expansion, Water Resour. Res., 49, 2664-2682, doi:10.1002/wrcr.20226.

Lander, R. H., and O. Walderhaug (1999), Predicting porosity through simulating sandstone compaction and quartz cementation, AAPG Bull., 83(3) 433-449.

Le Maitre, O., and O. Knio (2010), Spectral methods for uncertainty quantification, Scientific Computation, Springer.

Li, W., Z. Lu, and D. Zhang (2013), Stochastic analysis of unsaturated flow with probabilistic collocation method, Water Resour. Res., 49, W08425, doi:10.1029/2008WR007530.

Liao, Q., and D. Zhang (2013), Probabilistic collocation method for strongly nonlinear problems: 1. Transform by location, Water Resour. Res., 49, 7911-7928, doi:10.1002/2013WR014055.

Lin, G., and A. M. Tartakovsky (2009), An efficient, high-order probabilistic collocation method on sparse grids for three-dimensional flow and solute transport in randomly heterogeneous porous media, Adv. Water Resour., 34, doi:1527-1538, 10.1016/j.advwatres.2008.09.003.

McPherson, B.J.O.L., and J.D. Bredehoeft (2006), Overpressures in the Uinta basin, Utah: Analysis using a three-dimensional basin evolution model, Water Resour. Res., 37(4), 857-871, doi:10.1029/2000WR900260.

Milliken, K. L. (2004), Late diagenesis and mass transfer in sanstone-shale sequences, Treatise Geochem., 7, 115-158.

Müller, F., P. Jenny and D. W. Meyer (2011), Probabilistic collocation and lagrangian sampling for advective tracer transport in randomly heterogeneous porous media, Adv. Water Resour., 34, 1527–1538, doi: 10.1016/j.advwatres.2011.09.005.

Nelder, J. A., and R. Mead (1965), A simplex method for function minimization, The Computer Journal 7(4), 308-313, doi: 10.1093/comjnl/7.4.308.

Nobile, F., R. Tempone, and C. G. Webster (2008), An anisotropic sparse grid stochastic collocation method for partial differential equations with random input data, SIAM J. Numer. Anal., 46, 2411–2442, doi:10.1137/070680540.

Oelkers, E. H., P. A. Bjorkum, and W. M. Murphy (1996), A petrographic and computational investigation of quartz cementation and porosity reduction in North Sea sandstones, Am. J. Sci., 296, 420–452.

Oladyshkin, S., H. Class, and W. Nowak (2013), Bayesian updating via bootstrap filtering combined with data-driven polynomial chaos expansions: methodology and application to history matching for carbon dioxide storage in geological formations, Computat. Geosci., 17(4), 671-687, doi:10.1007/s10596-013-9350-6.

Osborne, M. J., and R. E. Swarbrick (1999), Diagenesis in North Sea HPHT clastic reservoirs consequences for porosity and overpressure prediction, Mar. Petrol. Geol., 16, 337-353, doi: 10.1016/S0264-8172(98)00043-9.

Riva, M., A. Guadagnini, S. P. Neuman, E. Bianchi Janetti, and B. Malama (2009), Inverse analysis of stochastic moment equations for transient flow in randomly heterogeneous media, Adv. Water Resour., 10, 271–280, doi: 10.1016/j.advwatres.2009.07.003.

Riva, M., M. Panzeri, A. Guadagnini, and S. P. Neuman (2011), Role of model selection criteria in geostatistical inverse estimation of statistical data and model parameters, Water Resour. Res., 47, W07502, doi: 10.1029/2011WR010480.

Saad, G., and R. Ghanem (2009), Characterization of reservoir simulation models using a polynomial chaos-based ensemble Kalman filter, Water Resour. Res., 45, W04417, doi:10.1029/2008WR007148.

Schneider, F., M. Bouteca, and G. Vasseur (1994), Validity of the porosity/effective stress concept in sedimentary basin modeling, First Break, 12, 321-326.

Sobol, I. M., (1991), Global sensitivity indices for nonlinear mathematical models and their Monte Carlo estimates, Math. Comput. Simulat., 55(1-3), 271–280, doi:10.1016/S0378-4754(00)00270-6.

Sochala, P., and O. Le Maitre (2013), Polynomial Chaos expansion for subsurface flows with uncertain soil parameters, Adv. Water Resour., 62, 139–154, doi: 10.1016/j.advwatres.2013.10.003.

Sudret, B., (2007), Global sensitivity analysis using polynomial chaos expansion, Reliab. Eng. Syst. Safety, 93(7), 964-979, doi:10.1016/i.ress.2007.04.002.

Taylor, T. R., M. R. Giles, L. A. Hathon, T. N. Diggs, N. R. Braunsdorf, G. V. Birbiglia, M. G. Kittridge, C. I. Macaulay, and I. S. Espejo (2010), Sandstone diagenesis and reservoir quality prediction: Models, myths, and reality, AAPG Bull., 94(8), 1093-1132, doi:10.1306/04211009123.

Tuncay, K., and P. Ortoleva (2004), Quantitative basin modeling: present state and future developments towards predictability, Geofluids, 4, 23-39, doi:10.1111/j.1468-8123.2004.00064.x.

Walderhaug, O. (1994), Precipitation rates for quartz cement in sandstones determined by fluid-inclusion microthermometry and temperature-history modeling, J. Sed. Resear, A64, 324–333.

Walderhaug, O. (1996), Kinetic modeling of quartz cementation and porosity loss in deeply buried sandstone reservoirs, AAPG Bull., 80, 731-745.

Wangen, M., (2010), Physical Principles of Sedimentary Basin Analysis. Cambridge University Press, Cambridge (UK).

Wieck, J., M. Pearson, and L. Strayer (1995), A finite element method for simulating fault block motion and hydrothermal fluid flow within rifting basins, Water Resour. Res., 31(12), 3241-3258, doi:10.1029/95WR02114.

Xiu, D., and J. Hestaven (2005), High-order collocation methods for differential equations with random inputs, SIAM J. Sci. Comput., 27, 1118-1139, doi:10.1137/040615201.

Xiu, D., and G. E. Karniadakis (2002), The Wiener–Askey polynomial chaos for stochastic differential equations, SIAM J. Sci. Comput., 24(2), 619-644, doi: 10.1137/S1064827501387826.

Zhang, G., D. Lu, M. Ye, M. Gunzburger, and C. Webster (2013), An adaptive sparse-grid high-order stochastic collocation method for Bayesian inference in groundwater reactive transport modeling, Water Resour. Res., 49, doi:10.1002/wrcr.20467.

Zhao, K., and I. Lerche (1993), Inversion of dynamical indicators in quantitative basin analysis models. II. synthetic tests and a case history using dynamical indicator tomography, Math. Geol., 25, 107-123, doi:10.1007/BF00893268.

TABLES

Parameter	$p_{n,min}$	$p_{n,max}$	$p_{n,true}$
β [Pa^{-1}]	4×10^{-8}	6×10^{-8}	5.8×10^{-8}
a_q [mol m^{-2} s^{-1}]	0.40×10^{-18}	3.56×10^{-18}	1.8×10^{-18}
G_T[K m^{-1}]	2.0×10^{-2}	4.0×10^{-2}	3.1×10^{-2}
h_{sea} [m]	400.0	600.0	520.0

Table 1. Selected uncertain parameters and associated a priori range of variability; $p_{n,true}$ indicates the parameter values used to generate the reference porosity and temperature fields.

	$\mathbf{\Phi}_0^* = \mathbf{\Phi}_{true}$	$\mathbf{\Phi}_1^*$	$\mathbf{\Phi}_2^*$	$\mathbf{\Phi}_3^*$	$\mathbf{\Phi}_4^*$	$\mathbf{\Phi}_5^*$	$\mathbf{T}_0^* = \mathbf{T}_{true}$	$\mathbf{T}_1^*$	$\mathbf{T}_2^*$	$\mathbf{T}_3^*$	$\mathbf{T}_4^*$	$\mathbf{T}_5^*$
σ_f	0	0.005	0.01	0.02	0.04	0.080	0	1.25 K	2.5 K	5 K	10 K	20 K
$\frac{\sigma_f}{\Delta f_{true}}$ [%]	0	0.96	1.92	3.84	7.68	15.36	0	0.93	1.86	3.72	7.44	14.88

Table 2. Standard deviations, σ_f, and normalized standard deviations, $\sigma_f / \Delta f_{true}$, associated with the calibration datasets.

	$\mathbf{\Phi}_0^*$				$\mathbf{T}_0^*$			
	$w = 3$	$w = 4$	$w = 5$	a-gPCE	$w = 3$	$w = 4$	$w = 5$	a-gPCE
η_β	1.03	0.98	1.01	1.01	1.06	0.97	1.01	1.01
η_{a_q}	0.65	1.25	0.93	0.99	0.96	1.01	0.99	1.01
η_{G_T}	0.91	1.08	0.95	1.00	1.01	0.99	1.00	1.00
$\eta_{h_{sea}}$	0.99	0.99	0.99	1.00	1.00	0.99	1.00	1.00
NLL	-401.9	-395.7	-392.7	-490.6	-209.0	-264.7	-339.1	-475.8
KIC	-252.5	-246.6	-244.7	-333.8	-47.1	-101.8	-163.8	-231.9
CPU[s]	7.7×10^3	2.2×10^4	5.3×10^4	7.6×10^3	7.8×10^3	2.2×10^4	5.4×10^4	7.6×10^3

Table 3. Ratios $\eta_{p_n} = \hat{p}_n / p_{n,true}$ obtained using $\mathbf{\Phi}_0^*$ or $\mathbf{T}_0^*$ according to gPCE with w = 3, 4, 5 and a-gPCE; associated minimum values of *NLL*, *KIC* as well as CPU time are also listed.

	$w = 3$	$w = 4$	$w = 5$	a-gPCE	FM
η_β	1.14	1.20	1.10	1.12	1.20
η_{a_q}	1.82	0.65	0.76	1.30	0.91
η_{G_T}	0.91	1.08	0.96	0.98	1.08
$\eta_{h_{sea}}$	1.17	1.20	1.14	1.15	1.30
$\hat{\sigma}_\phi / \sigma_\phi$	1.15	1.11	1.15	1.15	1.14

Table 4. Ratios $\eta_{p_n} = \hat{p}_n / p_{n,true}$ and $\hat{\sigma}_\phi / \sigma_\phi$, obtained with gPCE with w = 3, 4, 5, a-gPCE and the full model (FM). All results are obtained on the basis of dataset $\mathbf{\Phi}_3^*$.

	$\hat{\sigma}_{\phi}$	$\hat{\sigma}_{T}$	$\hat{\lambda}$
$\mathbf{\Phi}_1^*$	0.0047	–	–
$\mathbf{\Phi}_2^*$	0.0078	–	–
$\mathbf{\Phi}_3^*$	0.0230	–	–
$\mathbf{\Phi}_4^*$	0.0316	–	–
$\mathbf{\Phi}_5^*$	0.0751	–	–
$\mathbf{T}_1^*$	–	1.23	–
$\mathbf{T}_2^*$	–	2.29	–
$\mathbf{T}_3^*$	–	4.58	–
$\mathbf{T}_4^*$	–	9.14	–
$\mathbf{T}_5^*$	–	19.71	–
$\mathbf{\Phi}_1^*, \mathbf{T}_1^*$	0.0049	1.22	1.6×10^{-5}
$\mathbf{\Phi}_2^*, \mathbf{T}_2^*$	0.0080	2.30	1.2×10^{-5}
$\mathbf{\Phi}_3^*, \mathbf{T}_3^*$	0.0229	4.68	2.4×10^{-5}
$\mathbf{\Phi}_4^*, \mathbf{T}_4^*$	0.0317	9.17	1.2×10^{-5}
$\mathbf{\Phi}_5^*, \mathbf{T}_5^*$	0.0702	17.56	1.4×10^{-5}

Table 5. ML estimates of σ_{ϕ}, σ_{T} and λ obtained from the diverse datasets considered.

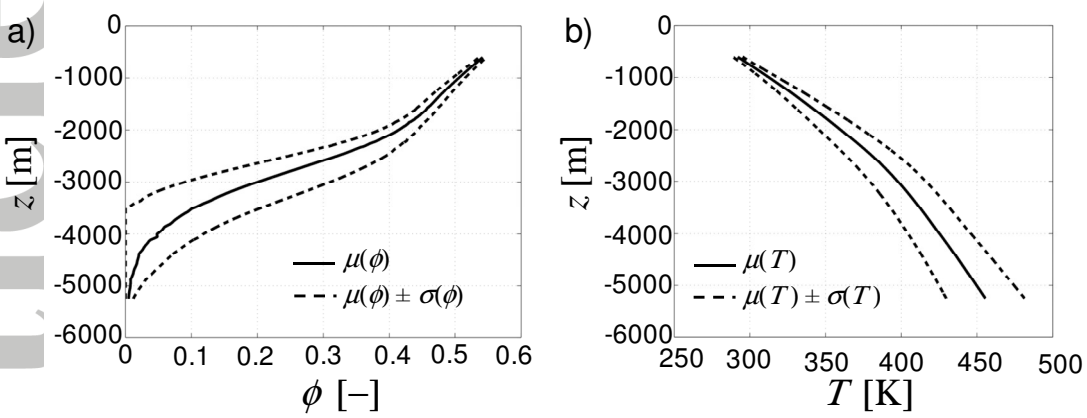

Figure 1. Vertical distribution of (a) mean porosity, $\mu(\phi)$, and (b) mean temperature, $\mu(T)$, (solid curves) at t = 200 Ma. Intervals corresponding to ± one standard deviation about the mean are also shown (dashed curves).

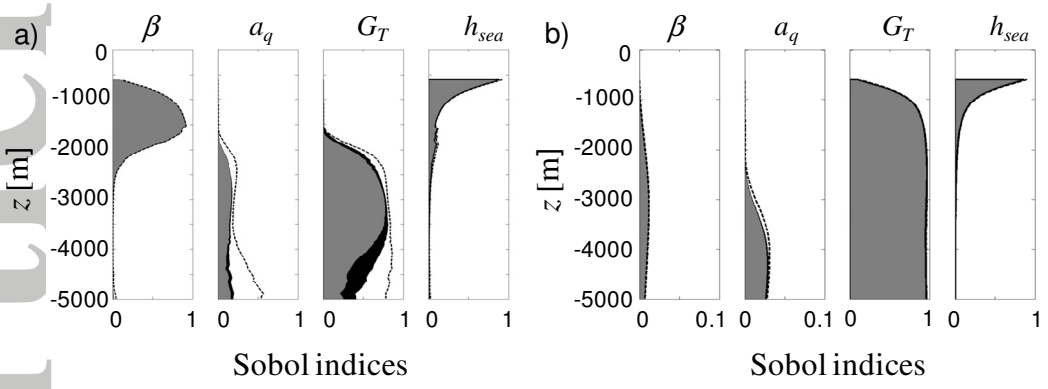

Figure 2. Sobol indices associated with (a) porosity and (b) temperature at t = 200 Ma: S_n^T (dashed curves), S_n (black shaded area), S_n^L (grey shaded area).

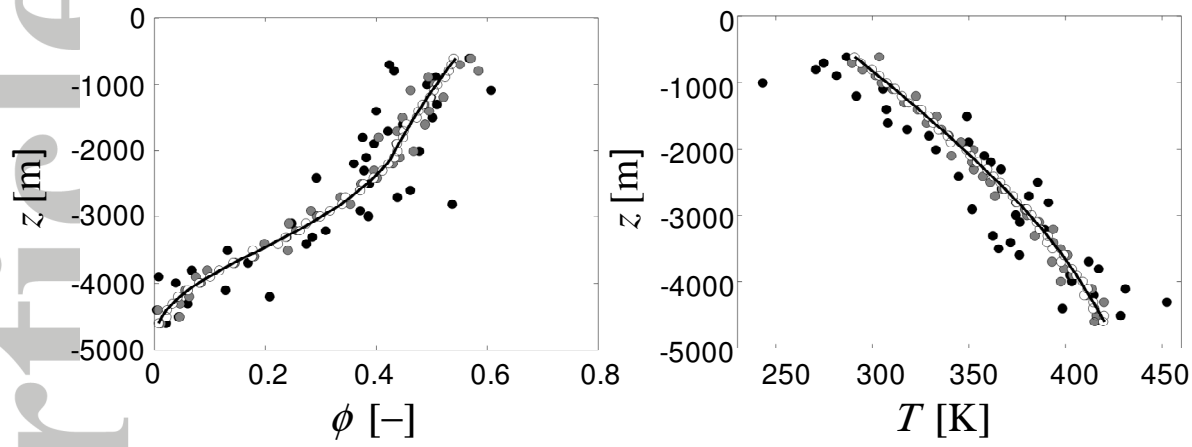

Figure 3. True (a) porosity and (b) temperature distributions along z at t = 200 Ma (continuous curves). Perturbed datasets are reported with symbols: $\mathbf{\Phi}_1^*, \mathbf{T}_1^*$ (white circles), $\mathbf{\Phi}_3^*, \mathbf{T}_3^*$ (grey circles), $\mathbf{\Phi}_5^*, \mathbf{T}_5^*$ (black circles).

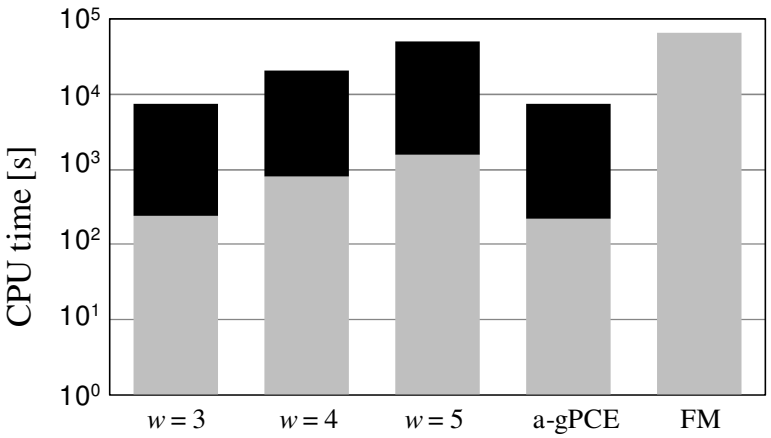

Figure 4. CPU time required for ML parameter estimation through dataset $\mathbf{\Phi}_3^*$ using gPCE, a-gPCE and the full model (FM). Grey and black areas indicate CPU time needed for the inversion procedure and to construct the surrogate model, respectively.

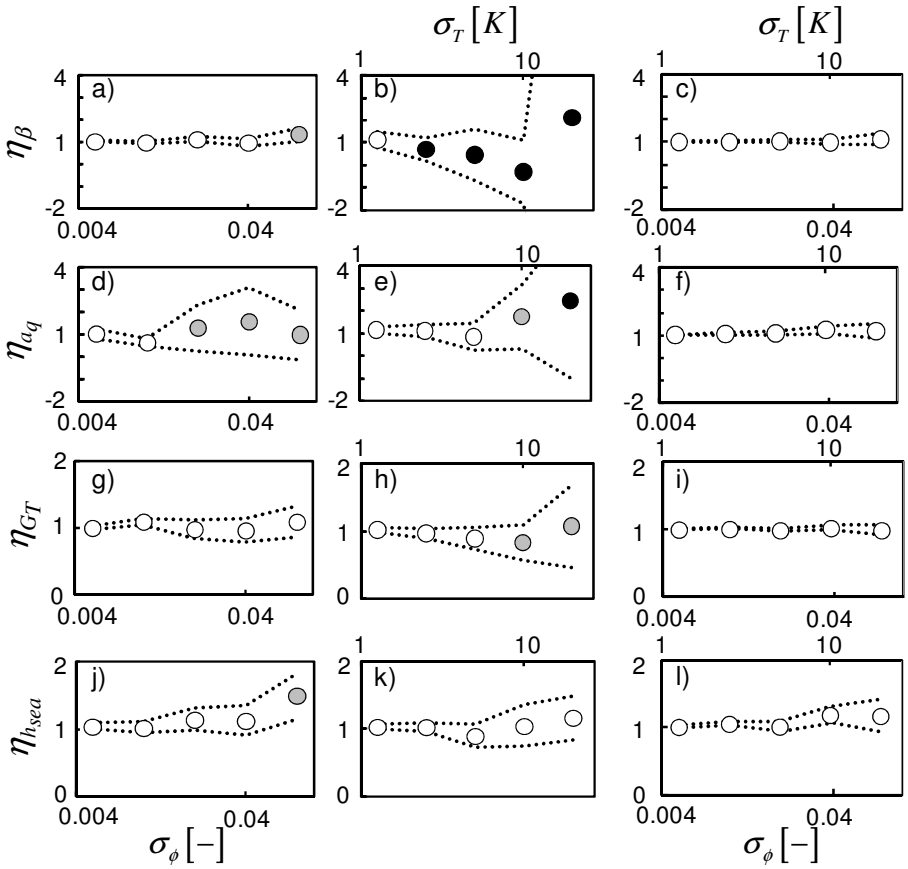

Figure 5. Normalized ML estimates of model parameters (a-c) η_β, (d-f) η_{a_q}, (g-i) η_{G_T},(j-l) $\eta_{h_{sea}}$ versus σ_ϕ (bottom horizontal axes) and/or σ_T (top horizontal axes). Results are obtained on the basis of porosity data only (a, d, g, j), temperature data only (b, e, h, k), and joint use of porosity and temperature data (c, f, i, l).

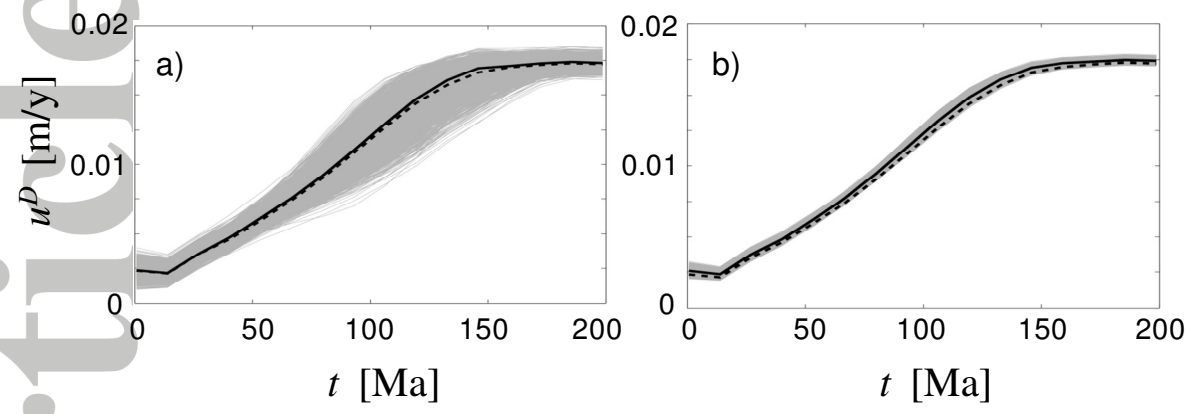

Figure 6. Time evolution of u^D at $z = -650\ m$: $u^D_{true}(t)$ (dashed curves), ML predictions (solid black curves) obtained using (a) $\mathbf{\Phi}_2^*$ and (b) $\left(\mathbf{\Phi}_2^*, \mathbf{T}_2^*\right)$ dataset. Grey curves represent u^D evaluated by a-gPCE on an ensemble of 5000 parameter realizations.

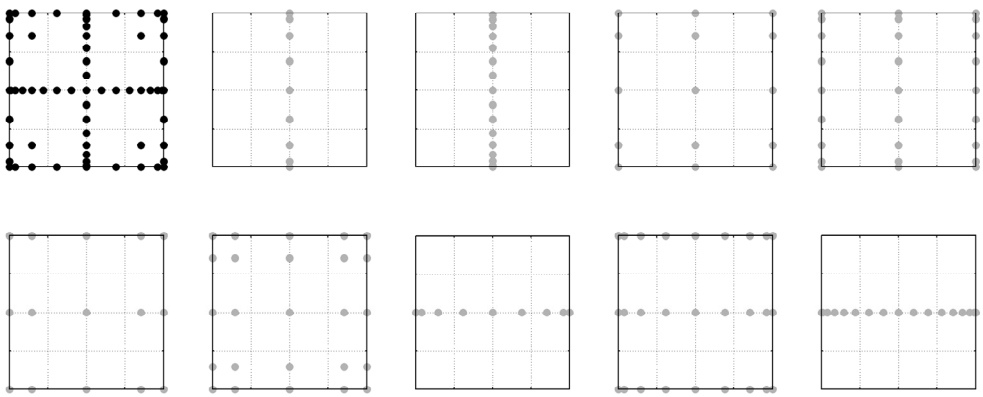

Figure A1. Graphical example of a sparse grid construction via superimposition of tensor grids: complete two-dimensional sparse grid (top left, black points) and related components (grey points).

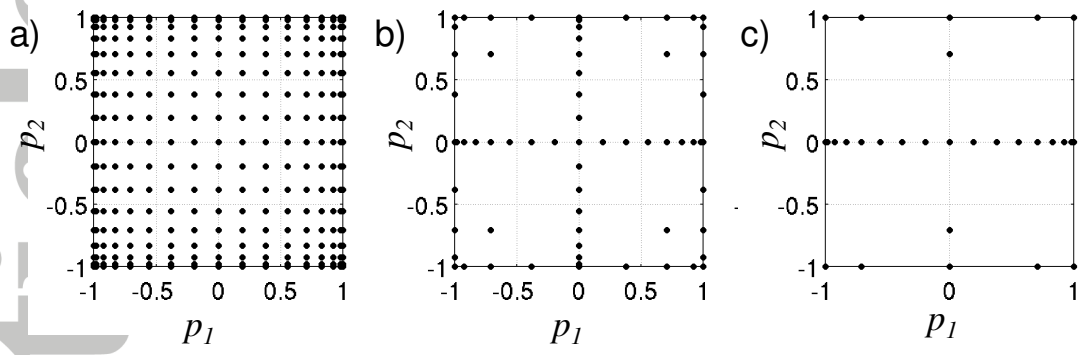

Figure A2. Three sampling strategies of a two-dimensional parameter space $\Gamma = [-1,1]\times[-1,1]$: (a) tensor grid; (b) isotropic sparse grid; (c) anisotropic sparse grid with refinement along the direction of parameter p_1.

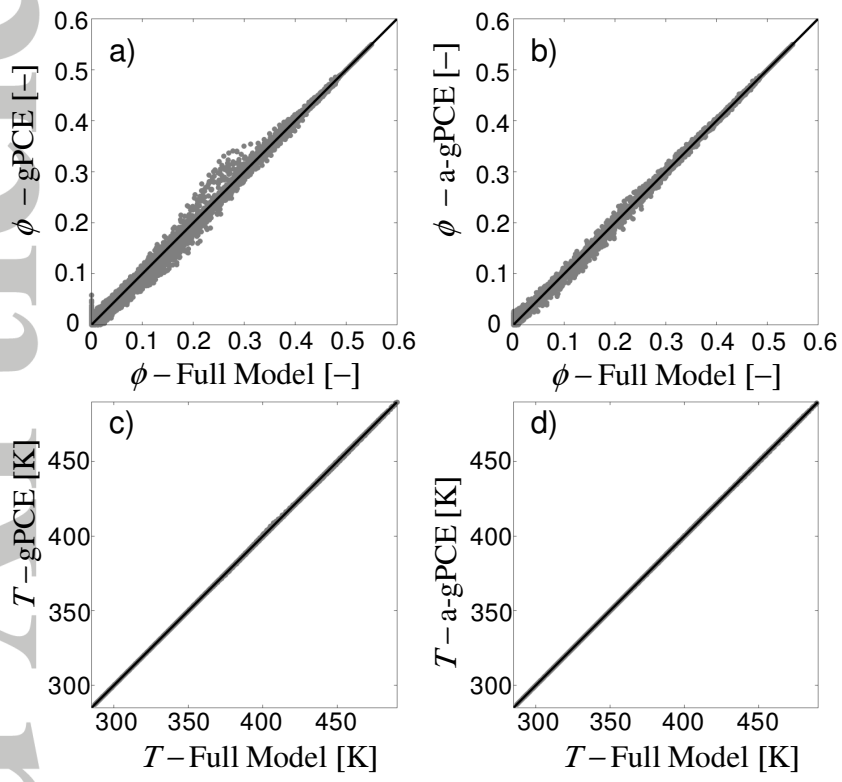

Figure B1. Scatterplots of porosity (a-b) and temperature (c-d) values obtained through gPCE with w = 3(a, c) and a-gPCE (b, d) versus full model outcomes. Results are associated with 500 randomly selected sets of parameters.